



Evaluating optical properties of real photonic crystal fibers with compressed sensing based on non-subsampled contourlet transform



Yan Shen, Jing Liu, Shuqin Lou ^{*}, Ya-Li Hou, Houjin Chen

School of Electronic and Information Engineering, Beijing Jiaotong University, Beijing 100044, China

HIGHLIGHTS

- Based on compressed sensing with non-subsampled contourlet transform (NSCT) and the total variation model, an effective method is proposed to evaluate the optical properties of real photonic crystal fibers (PCF).
- The cross section images of real PCFs are rebuilt effectively by using only 36% image data.
- Optical properties of commercial PCFs are evaluated efficiently without requirement of expensive apparatus and long samples.

ARTICLE INFO

Article history:

Received 25 December 2016

Revised 2 April 2017

Accepted 3 April 2017

Available online 5 April 2017

Keywords:

Non-subsampled contourlet transform (NSCT)

Photonic crystal fiber

Compressed sensing

Optical properties

ABSTRACT

A real photonic crystal fibers (PCFs) evaluation approach based on compressed sensing with non-subsampled contourlet transform (NSCT) and the total variation model is proposed for modeling optical properties of the real PCFs. The classical images of a commercial large mode area PCF and polarization-maintaining PCF are used to verify the effectiveness of the proposed method. Experimental results demonstrate that the cross section images of real PCFs are rebuilt effectively by using only 36% image data for evaluating the optical properties with the same accuracy as by 100% data. To the best of our knowledge, this is the instance of applying the compressed sensing with the NSCT and total variation to reconstruct the cross section images of PCFs for quickly evaluating the optical properties of real PCFs without the requirement of long fiber samples and expensive measurement apparatuses.

© 2017 Elsevier B.V. All rights reserved.

1. Introduction

Photonic crystal fibers (PCFs) have the advantages of novel optical properties and flexible structures [1]. Various PCFs with unique optical properties are developed for fiber device, optical communication, fiber sensor, and so on [2–4]. The accurate evaluation of optical properties is very important for the application of PCFs [5–7].

Generally, the optical properties of PCFs can be evaluated by the direct method and indirect method. The direct method requires long samples and expensive measurement apparatuses. Therefore several indirect methods are reported to evaluate optical properties of real PCFs and to assist in the fabrication of PCFs in the initial stage. Fokoua proposed an indirect method to evaluate optical properties of PCFs by extracting the coordinates of cross sections of PCFs [8,9]. Wang [10] built a low-coherence interferometry to measure the group velocity dispersion of three kinds of hollow-

core photonic bandgap fibers (HC-PBGFs) indirectly. Napoerala et al. extracted the fiber structure from the electron microscope image and then used the finite difference method to evaluate the optical properties of their fabricated PCFs [11]. This indirect method, which rebuilt the geometry of PCFs and utilized the theoretical analysis model to obtain the fiber properties, has the advantages of low cost, wide applicability, and capability for rapidly evaluating fiber properties.

Our group has proposed an indirect method to evaluate optical properties of real PCFs. The method combines the digital image processing technique and full-vector finite element method (FEM) [12–14]. The results obtained are in accordance with the direct measurement results.

During the fabrication of PCFs, we need to sample multiple cross sections of PCFs and evaluate the optical properties of the PCFs sample to determine whether it is in accordance with the design. The evaluating results can be used to adjust the fabrication parameters and determine the uniformity of the PCFs sample [12]. This process will generate many cross section images of PCFs. It is very important to reconstruct the cross section images and then

^{*} Corresponding author.

E-mail address: shqlou@bjtu.edu.cn (S. Lou).

evaluate the optical properties rapidly with small amount of image data.

Compressed sensing (CS) is a new sampling theory only requiring a small amount of data via a tractable convex optimization approach [15,16]. If we want to use CS to reconstruct the cross section images of PCFs by a small amount of cross section data with sound reconstruction quality, we need to find a much sparser representation of the image and meanwhile preserve the detailed shape of the image. The conventional Fourier and wavelet transform of the image cannot give the sparsest representation and can only give three directions of the decomposition of the image. However, for a certain image, the non-subsampled contourlet transform (NSCT) offers a much sparser representation than the Fourier and wavelet transform do [17]. Furthermore, NSCT is an effective representation for the images with contour shapes and keeps the image features with multi-scales and multi-directions. NSCT has the property of shift-invariant that preserves the detailed information of images in different directions, and thus overcomes the shift-variant of the contourlet transform, which introduces the artifacts during the decomposition and reconstruction process. Therefore, NSCT is a relatively preferable representation for the cross section images of PCFs which include some regular circle shapes.

In this paper, we propose an evaluation method of optical properties of PCFs with NSCT-based compressed sensing for reconstructing the cross sections of PCFs with relatively less data and meanwhile preserving the edge detail information of cross section images of PCFs. There is still some noise in the cross section images of PCFs although rebuilt by NSCT-based CS. Many researchers have been devoted to this denoising issue. Total variation (TV) has been a very effective denoising method up to now [18,19]. Therefore the TV model will be adopted to denoise the cross section images of PCFs reconstructed by the NSCT-based CS.

2. The proposed method

The proposed evaluation method combines NSCT-based CS and TV to rebuild the cross section images of PCFs with a small amount of cross section image data. The optical properties of two kinds of PCFs produced by the Crystal Fiber A/S are evaluated by using full-vector FEM to validate the effectiveness of the proposed method. To the best of our knowledge, this is the first instance of applying the NSCT-based CS and TV to reconstruct the cross section images of PCFs for evaluating the optical properties of real PCFs.

Fig. 1 shows the flow chart of evaluating optical properties of real PCFs by the proposed method. The proposed evaluating method includes several key steps. The first key step is the “Data sampling by compressed sensing” (i.e., the cross section images of PCFs are down-sampled by NSCT-based compressed sensing). The second key step is the “Rebuild of the cross section of PCF by NSCT-based CS” with the split Bregman iteration. The third key step is the “TV denoising”, which suppresses the noise generated by previous steps. After threshold estimation and binary processing, air holes filling, the edges of air holes in the cross section

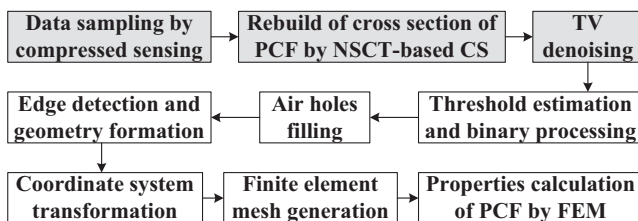


Fig. 1. Flow chart of evaluating optical properties of real PCFs.

images are detected and the geometry is formed. Finally, we transform the coordinate system and adopt the FEM to evaluate the optical properties of real PCFs.

2.1. The non-sampled contourlet transform

The non-sampled contourlet transform (NSCT) is an effective sparse representation for images with contours in different directions [17]. Compared with contourlet transform, NSCT has the property of shift-invariance, which will reduce the pseudo-Gibbs phenomena around singularities. For the cross section image of a PCF, it is composed of multiple air holes with contours in different directions. Therefore, NSCT can detect the features of cross section images along contours at multiple scales, locations and directions.

The cross section image of a PCF can be decomposed into multi-scale subband images by a non-subsampled pyramid (NSP) filter for capturing the point discontinuities, followed by a non-subsampled directional filter bank (NSDFB) for linking point discontinuities into linear structures and capturing the features of the contours of the image. The structures of the filters are shown in Fig. 2.

The input image $x, x \in L_2(Z^2)$, shown in Fig. 2(a), is decomposed into the low frequency subband $a_j[n]$ by convolving with the low-pass filter function $h_{j,0}[n]$ of NSP filter and into the band-pass frequency subband $b_j[n]$ by convolving with the band-pass filter function $h_{j,1}[n]$. The scale parameter $j(j \in Z^+)$ represents the decomposition levels of scales of the cross section image, where J is a

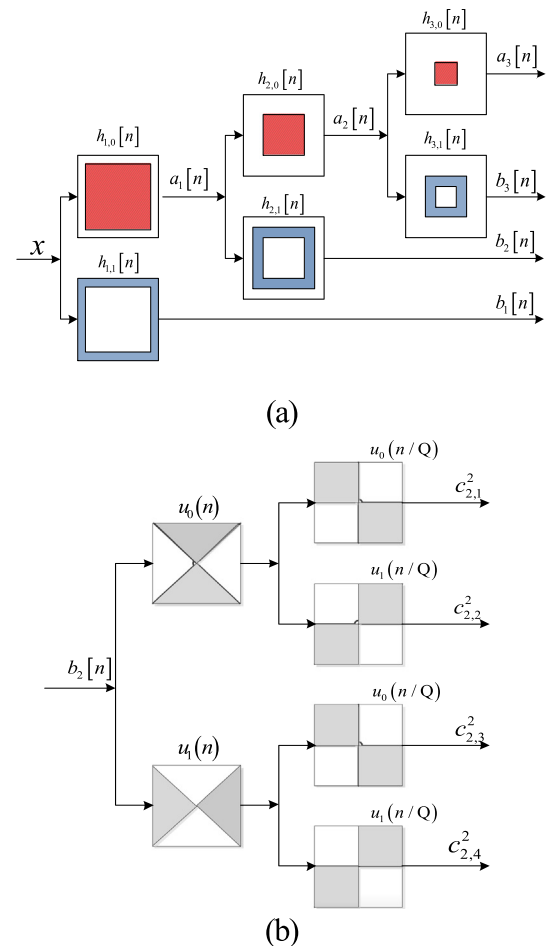


Fig. 2. Non-subsampled contourlet transform. (a) Three-stage decomposition of NSP. (b) Four directional decomposition of NSDFB with two-channel fan filter banks.

positive integer greater than 2, $j = 1, 2, \dots, J$. The location parameter n represents the coordinate position in horizontal and vertical directions, $n \in \mathbb{R}^2$. Then the band-pass frequency subband $b_j[n]$ is divided into multiple directions $c_{j,k}^l[n]$ by convolving with the directional filter function $u_{j,k}^l[n]$ of the NSDFB filter, as shown in Fig. 2(b). The direction parameter k denotes the pass-band frequency subband $c_{j,k}^l[n]$ in different directions, $k = 0, 1, 2, \dots, 2^j - 1$ and $a_j[n]$ is the low frequency coefficient in the last scale decomposition level. The decomposition of x can be expressed as

$$x = \sum_n a_j[n] h_j[n] + \sum_j \sum_n \sum_k c_{j,k}^l[n] \lambda_{j,k}^l[n] \quad (1)$$

$$a_j[n] = \langle x, h_j[n] \rangle, c_{j,k}^l[n] = \langle x, \lambda_{j,k}^l[n] \rangle$$

where $\lambda_{j,k}^l[n] = h_{j,1}[n] * (h_{j-1,0}[n] * \dots * h_{1,0}[n]) * u_{j,k}^l[n]$, “*” is the convolution operator. The direction level in the band-pass frequency subband denotes l_j . For example, if $j = 2$, $l_j = 2$, there are $k = 2^{l_j} = 4$ directions totally in the band-pass frequency subbands. The NSDFB filter can be expressed as $\lambda_{2,k}^2[n] = h_{2,1}[n] * h_{1,0}[n] * u_{2,k}^2[n]$, where $u_{2,1}^2[n] = u_0[n] * u_0[n/Q]$, $u_{2,2}^2[n] = u_0[n] * u_1[n/Q]$, $u_{2,3}^2[n] = u_1[n] * u_0[n/Q]$, $u_{2,4}^2[n] = u_1[n] * u_1[n/Q]$, where Q is the down-sampling factor. Combining Fig. 2(a) with Fig. 2(b), the whole decomposition process of NSCT can be summarized in Fig. 3.

After the process of NSP and NSDFB, the image can be decomposed into subbands with multi-scale and multi-direction. Each subband contains the information of some direction of the image. Therefore, the image is sparse in the NSCT domain.

2.2. NSCT-based compressed sensing

Compressed sensing (CS) can reconstruct a high-dimensional sparse signal from a small number of linear non-adaptive measurements [20] by

$$y = \Phi x + z \quad (2)$$

where Φ is an $m \times n$ sensing matrix with $m < n$, x is a $n \times 1$ vector, z is the noise term modeling measurement error, $z \in \mathbb{R}^m$. We aim at reconstructing the cross section image x of a PCF from the available measurement y . The cross section image x has a much sparser representation in the NSCT domain than in the wavelet transform domain. It can be denoted by the equation $x = Ds$, $D \in \mathbb{R}^{n \times d}$ ($n < d$), where D is the NSCT transform matrix. Therefore Eq. (2) can be written as

$$y = \Phi x + z = \Phi Ds + z = \Psi s + z \quad (3)$$

where $\Psi = \Phi D$, s is a sparse coefficient vector, $s \in \mathbb{R}^d$. The vector Ψs means selecting some coefficients randomly from s as the compressed vector y . Therefore the CS model can be described as

$$\hat{x} = \operatorname{argmin}_{x \in \mathbb{R}^n} \|D^* x\|_1 \text{ s.t. } \|y - \Phi x\|_2 \leq \varepsilon \quad (4)$$

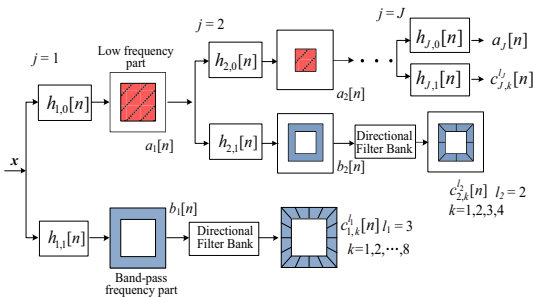


Fig. 3. The decomposition process of NSCT in multi-scales and multi-directions.

where ε is a likely upper bound on the noise power. We can change the constrained Eq. (4) into the unconstrained Eq. (5)

$$\hat{x} = \operatorname{argmin}_{x \in \mathbb{R}^n} \lambda \|D^* x\|_1 + \frac{1}{2} \|y - \Phi x\|_2^2 \quad (5)$$

We decompose the NSCT transform matrix D into

$$D = (DD^*)^{-1} D + W^* (I_d - D^* (DD^*)^{-1} D) = \bar{D} + W^* P \quad (6)$$

where $\bar{D} = (DD^*)^{-1} D$, $P = I_d - D^* (DD^*)^{-1} D$, W is an arbitrary matrix. Here we use the optimal-dual-based l_1 -analysis method to recover the image x directly from the optimization model in Eq. (5). This method works well for the reconstruction of the image with regular shapes [21]. We substitute Eq. (6) into Eq. (5) and obtain Eq. (7) as below

$$\hat{x} = \operatorname{argmin}_{x \in \mathbb{R}^n, g \in \mathbb{R}^n} \lambda \|\bar{D}^* x + Pg\|_1 + \frac{1}{2} \|y - \Phi x\|_2^2 \quad (7)$$

where $g = Wx$. The optimization process is not only over the signal space but also over all dual frames of D .

Eq. (7) is non-smooth and non-separable, so we adopt the split Bregman method to solve this optimal problem. Then Eq. (7) is transformed into

$$(x^{k+1}, g^{k+1}) = \operatorname{argmin}_{x, g} \{ \frac{\gamma}{2} \|\bar{\Psi}^* x + Pg\|_1 + \frac{\gamma}{2} \|\Phi x - y + c^k\|_2^2 \} \quad (8)$$

$$c^{k+1} = c^k + (\Phi x^{k+1} - y) \quad (9)$$

Eq. (8) can be decomposed into three sub-problems by minimizing iteratively x , d , and g respectively, as shown in Eqs. (10)–(13).

$$x^{k+1} = \operatorname{argmin}_x \left\{ \frac{\gamma}{2} \|\Phi x^k - y + c^k\|_2^2 + \frac{\gamma}{2} \|\bar{\Psi}^* x^k + Pg^k - d^k + b^k\|_2^2 \right\}, \quad (10)$$

$$d^{k+1} = \operatorname{argmin}_d \left\{ \frac{\gamma}{2} \|\Phi x^{k+1} - y + c^k\|_2^2 + \|\bar{d}^k\|_1 + \frac{\gamma}{2} \|\bar{\Psi}^* x^{k+1} + Pg^k - d^k + b^k\|_2^2 \right\}, \quad (11)$$

$$g^{k+1} = \operatorname{argmin}_g \left\{ \frac{\gamma}{2} \|\bar{\Psi}^* x^{k+1} + Pg^k - d^{k+1} + b^k\|_2^2 \right\}, \quad (12)$$

$$b^{k+1} = b^k + (\bar{\Psi}^* x^{k+1} + Pg^{k+1} - d^{k+1}). \quad (13)$$

Combining these three steps (Eqs. (10)–(12)) with the update of b^k (Eq. (13)) and c^k (Eq. (9)), we solve the sub-problems involved in Eq. (8) with the appropriate iterations. The detailed process can be seen in Ref. [20]. The reconstructed cross section image \hat{x} is obtained after the above process.

The under-sampling ratio δ is defined as the number of sampled measurements m divided by the total pixels n of the image, $\delta = m/n$, which is the criterion to judge the results of compressed sensing. Lower δ means we need less data to reconstruct the original image.

2.3. The denoising model of total variation

The cross section images of PCFs are unavoidably contaminated by noises in the photographing and the compressed sensing step. Therefore the denoising step is important for extracting the edge of air holes.

Total variation is an effective model that can recover the noisy image with well-preserved edges. The noisy image after compressed sensing is f , $f = \hat{x}$. The image regression model is

$$f = u + v \quad (14)$$

where u is the desired clean image and v is the Gaussian white noise. A common way to solve Eq. (14) is to add a TV penalized term $\rho_{TV}(u)$

$$\hat{u} = \operatorname{argmin}_u \frac{1}{2} \|f - u\|_2^2 + \alpha \rho_{TV}(u) \quad (15)$$

where α is a positive regularization parameter, ∇_h and ∇_v denote the horizontal and vertical difference operators, respectively.

$$\rho_{TV}(u) = \|\sqrt{(\nabla_h u)^2 + (\nabla_v u)^2}\|_1 \quad (16)$$

Split Bregman iteration is adopted to convert the non-separable problem of Eq. (15) into a problem involving only separable terms. We replace the differential term in Eq. (15) with a new variable e , $e = \nabla u$. Hence, Eq. (15) can be written as

$$\hat{u} = \operatorname{argmin}_u \frac{1}{2} \|f - u\|_2^2 + \alpha \|e\|_1 \quad \text{s.t.} \quad e = \nabla u \quad (17)$$

By introducing e , the constrained problem of Eq. (17) is changed into the unconstrained Eq. (18).

$$\hat{u} = \operatorname{argmin}_u \frac{1}{2} \|f - u\|_2^2 + \alpha \|e\|_1 + \frac{\beta}{2} \|e - \nabla u - h\|_2^2 \quad (18)$$

where h is a variable related to the Bregman iteration algorithm, β is a penalty parameter. In each step, either e or u is minimized while the other variables are fixed.

$$u^{k+1} = \operatorname{argmin}_u \frac{1}{2} \|u^k - f\|_2^2 + \frac{\beta}{2} \|\nabla u^k - e^k + h^k\|_2^2 \quad (19)$$

$$e^{k+1} = \operatorname{argmin}_e \alpha \|e^k\|_1 + \frac{\beta}{2} \|e^k - \nabla u^{k+1} - h^k\|_2^2 \quad (20)$$

$$h^{k+1} = h^k + \nabla u^{k+1} - e^{k+1} \quad (21)$$

Eqs. (19)–(21) are the steps for solving the TV denoising problem of Eq. (17). The detailed steps can be referenced in [19]. After these steps, the clean cross section image of PCF is obtained and the following FEM can be applied to evaluate the optical properties of real PCFs.

2.4. The steps of the proposed algorithm

There are three main steps for implementing the evaluation of optical properties by the proposed method according to the above analysis.

Step I: Set up the compressed sensing model with the NSCT transform by Eqs. (3) and (4). The size of the input image is 64×64 pixels and δ changes from 30% to 36%. Select the NSP decomposition level $j = 1, 2$. Set the NSDFB decomposition level $l_j = 3$ ($j = 1$) with 8 directions and $l_j = 2$ ($j = 2$) with 4 directions. Solve Eqs. (10)–(13) and (9) with the original parameters: $x^0 = \mathbf{0}$, $d^0 = b^0 = Pg^0 = \mathbf{0}$, $c^0 = \mathbf{0}$, $\gamma = 1$, $\lambda = 1$, $\mathbf{0}$ is the zero vector. If $\|x^{k+1} - x^k\| \leq 10^{-3}$, the iteration is stopped and the denoised cross section image \hat{x} of PCF is obtained.

Step II: Set up the total variation model of Eq. (15) to denoise the cross section image f of PCF, $f = \hat{x}$. Split Bregman iteration is used to solve Eq. (17) with the initial parameters: $u^0 = \mathbf{0}$, $h^0 = \mathbf{0}$, $e^0 = \mathbf{0}$, $\alpha = 7$, $\beta = 5$. If $\|u^{k+1} - u^k\| \leq 10^{-3}$, the iteration will be stopped and the denoised cross section image of PCF \hat{u} is obtained.

Step III: From the rebuilt cross section image \hat{u} of PCF, we extract the edges of air holes by setting the threshold and filling air holes in Fig. 1. Then FEM is employed to compute the optical properties of PCFs.

3. Experimental results and analysis

Numerical experiments are carried out with the classical images and the cross section images of the commercial PCFs to validate the effectiveness of the proposed method.

3.1. Experimental results of classical images

The reconstructed results of the proposed method with classical images are shown in Fig. 4. The images from left to right in Fig. 4 are the reconstructed images with δ of 30%, 32%, 34% and 36%, respectively.

It can be observed from Fig. 4 that the restored images by the proposed method with 30% data shown in Fig. 4(a) and (e) are restored in low quality because the 30% sampling data used for restoring are not enough for preserving the edge information, which results in much noise and distortion in the image.

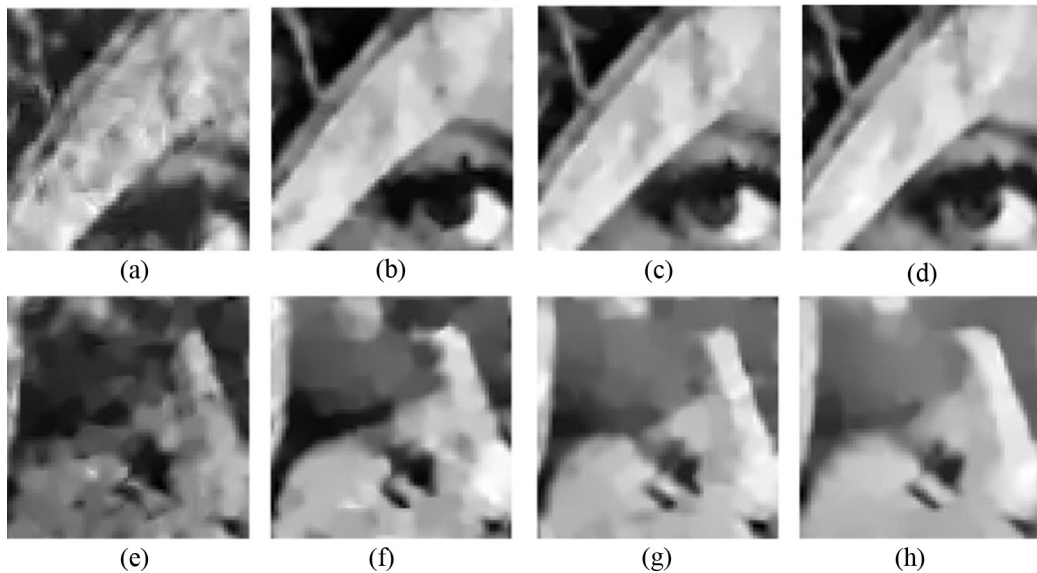


Fig. 4. Denoising results of classical images by NSCT-based compressed sensing and TV method where δ is 30% (a) and (e), 32% (b) and (f), 34% (c) and (g), and 36% (d) and (h).

The image quality of Fig. 4(b) and (f) with 32% data has a sharp improvement from Fig. 4(a) and (e) with 30% data. The quality of the reconstructed image is improved with the increase of the sampling ratio δ . Fig. 4(d) and (h) reconstructed with 36% data have much clearer eye browns and pepper edges than the images reconstructed with 30%, 32% and 34% data.

3.2. Experimental results of cross section images of PCFs

Fig. 5(a) and (b) shows the cross section images of a large mode area PCF and a polarization maintaining PCF, which are the products of the Crystal Fiber A/S [15].

Fig. 6(b) and (f) (with 32% data) are much clearer than Fig. 6(a) and (e) (with 30% data) in that most of the noise is suppressed. The reconstructed image with 32% data has a sharp increase in the image quality from the reconstructed images with 30% data. Therefore 32% is the critical point of the compressed sensing for cross section images of PCFs.

The reconstructed cross section images of PCFs with 34% data shown in Fig. 6(c) and (g) have clearer edges, better contrast and less noise than those with 32% data shown in Fig. 6(b) and (f).

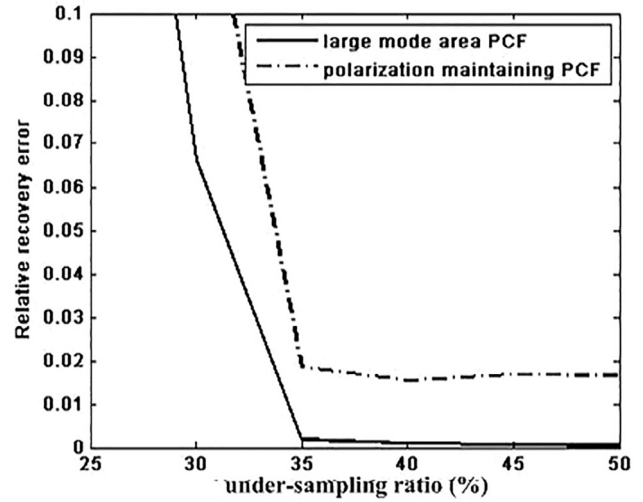


Fig. 7. Comparison of the relative recovery error of PCFs versus the under-sampling ratio.

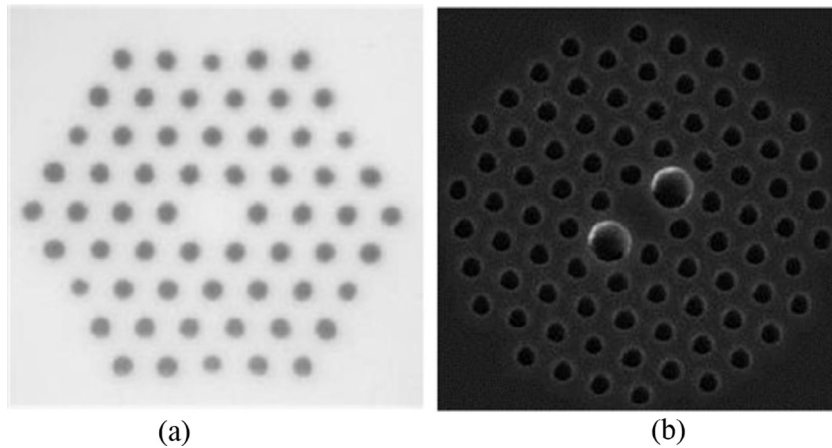


Fig. 5. Cross section images of several real PCFs. (a) Large mode area PCF, (b) polarization maintaining PCF.

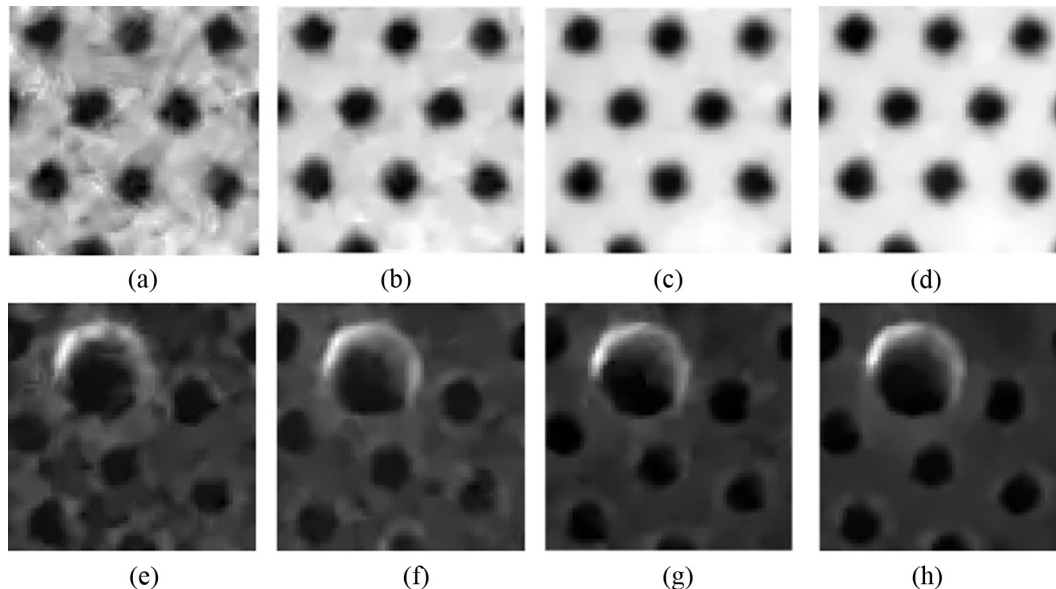


Fig. 6. Results of compressed sensing with contourlet transform and TV denoising where δ is 30% (a) and (e), δ is 32% (b) and (f), δ is 34% (c) and (g), and δ is 36% (d) and (h) of the zoomed images of PCFs in Fig. 5.

Fig. 6(d) and (h) are the reconstructed cross section images with 36% data. They have much clearer edges than Fig. 6(c) and (g) with 34% data. Therefore, 36% data is the appropriate sampling ratio to reconstruct the images by NSCT-based CS.

For testing the performance of the proposed method, the relative recovery error η is defined as

$$\eta = \|\hat{u} - u\|_2 / \|u\|_2 \quad (22)$$

where u is the original image, \hat{u} is the reconstructed image after compressed sensing and TV denoising. The relative recovery error η shows the approximation degrees of the reconstructed image to the original image with respect to the under-sampling fraction δ .

Fig. 7 is the comparison of the relative recovery error of PCFs with the increase of δ ranging from 30% to 36%. The relative recovery error η decreases with the increase of δ because higher δ means more cross section data are used to implement the compressed sensing, which ensures better reconstruction of the cross section image. When δ is below 30%, the relative recovery error η increases and the quality of reconstructed cross section images is worse with serious noise and distorted air holes. When δ is greater than 36%,

the relative recovery error η decreases and closes to zero. Figs. 4 and 6 show that 36% data can generate good quality of cross section images by the proposed method, which satisfies the demand for evaluation of optical properties of PCFs.

The reconstruction of cross section images of PCFs utilizing 36% data instead of 100% data requires less memory and a lower sampling rate during the photographing process. Next, experiments are carried out on the comparison of the reconstructed results by 36% and 100% data using the proposed methods.

Fig. 8 shows the reconstructed image with δ of 36% and 100% respectively. Fig. 8(a) and (b) are the images restored by the compressed sensing and TV denoising method with 36% data, which is very close to the images restored with 100% data shown in Fig. 8(c) and (d). By comparing the reconstruction results, it can be concluded that 36% data gives satisfactory reconstruction quality, which is as good as the 100% data does in preserving the edge detailed information of cross section images of PCFs.

Experimental results confirm that the proposed NSCT-based compressed sensing can reconstruct the cross section image with 36% data and obtain satisfactory sharp edges.

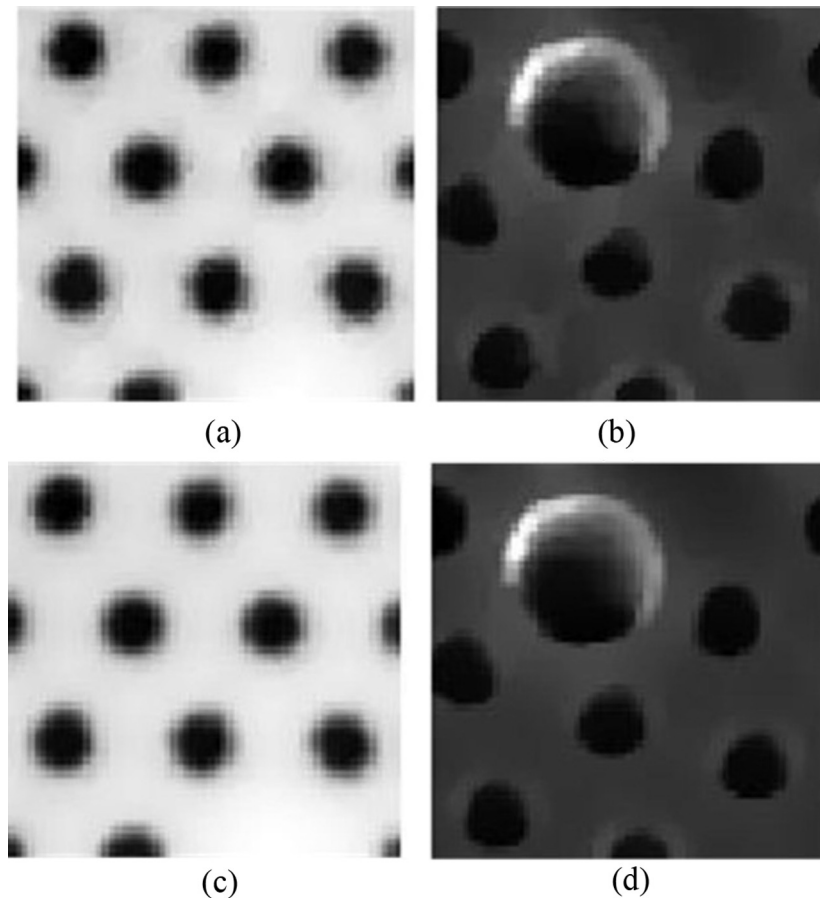


Fig. 8. The comparison of reconstruction of PCFs with $\delta = 36\%$ data of (a) and (b), with 100% data of (c) and (d).

Table 1
Mode field diameter of the fundamental mode.

Wavelength (μm)	0.4	0.6	0.8	1.0
Given results	4.2 ± 0.5			
Proposed results	4.029	4.098	4.136	4.201

Table 2

Comparison of numerical results with product parameters of the polarization-maintaining PCF.

$\lambda = 1550$ nm	Dispersion of two polarizations (ps/nm/km)		Beat length (mm)
Given results	54	59	<4
Proposed results	53.55	58.64	3.38

4. Evaluation of optical properties of PCFs

The finite element method is employed to calculate the optical properties of PCFs by using cross section images after edge extraction. The FEM has the advantage of simulating complex fiber structures with higher accuracy.

With the FEM, fiber characteristic parameters such as mode filed area, dispersion and beat length can be calculated through the refractive index distribution of the fiber cross sections [22].

The properties of PCFs can be modeled with FEM after the finite element mesh generation. With regard to the large mode area PCF [13], Table 1 gives the numerical results by the proposed method and the product data given by the Crystal Fiber A/S. Table 1 shows that the mode field area of the fundamental mode calculated by the proposed method agrees with the product data given by the Crystal Fiber A/S. With regard to the polarization maintaining PCF, the dispersion and beat length at the wavelength of 1550 nm are modeled, and the numerical results by the proposed method as well as the given results [13] by the Crystal Fiber A/S are listed in Table 2.

Table 2 shows that the dispersions of two polarizations from the proposed method are 53.55 ps/nm/km and 58.64 ps/nm/km respectively, which are approximate to the given results of 54 ps/nm/km and 59 ps/nm/km. The beat length 3.38 mm from the proposed method is also in the range of the given results (<4 mm). Numerical analysis results demonstrate that the proposed method can effectively evaluate the optical properties of real PCFs with high accuracy.

5. Conclusion

A novel evaluation method of evaluating PCFs' optical properties with NSCT-based compressed sensing is proposed to rebuild the cross section images of PCFs with 36% data of the cross section image. The cross section images of the real PCFs made by Crystal Fiber A/S companies are used to validate the proposed method. Experimental results show that the proposed method can rebuild the cross section image with only 36% data and preserve the edge details of air holes in multi-scales and multi-directions.

Acknowledgments

This work was supported in part by National Natural Science Foundation of China under Grant [grant numbers 61475016, 61301184, 61571036], Beijing Natural Science Foundation under Grant [grant number 4154083], Fundamental Research Funds for the Central Universities of China under Grant [grant number 2015JBM023].

References

- [1] J.C. Knight, T.A. Birks, P.S. Russell, et al., All-silica single-mode optical fiber with photonic crystal cladding, *Opt. Lett.* 21 (19) (1996) 1547–1549.
- [2] T.J. Yang, Y.F. Chau, H.H. Yeh, et al., Dispersion properties, birefringence and confinement loss of rotational elliptic air-hole photonic crystal fiber, *Appl. Phys. A* 104 (3) (2011) 857–861.
- [3] H. Gong, H. Song, S. Zhang, et al., Curvature sensor based on hollow-core photonic crystal fiber sagnac interferometer, *Sens. J. IEEE* 14 (3) (2014) 777–780.
- [4] D.C. Jones, C.R. Bennett, M.A. Smith, et al., High-power beam transport through a hollow-core photonic bandgap fiber, *Opt. Lett.* 39 (11) (2014) 3122–3125.
- [5] S.Q. Lou, W.L. Lu, X. Wang, A novel bend-resistant large-mode-area photonic crystal fiber, *Acta Phys. Sin. – Chin. Ed.* 62 (4) (2013) 044201–044209.
- [6] D. Wu, Y. Zhao, H.F. Hu, Experimental research on FLM temperature sensor with an ethanol-filled photonic crystal fiber, *Sens. Actuat. A* 209 (2014) 62–67.
- [7] F. Tian, Z. He, H. Du, Numerical and experimental investigation of long-period gratings in photonic crystal fiber for refractive index sensing of gas media, *Opt. Lett.* 37 (3) (2012) 380–382.
- [8] E.N. Fokoua, S.R. Sandoghchi, Y. Chen, Accurate Loss and Surface Mode Modeling in Fabricated Hollow-Core Photonic Bandgap Fibers, *OFC2014*, 2014, pp. OSAM2F.5.
- [9] E.N. Fokoua, S.R. Sandoghchi, Y. Chen, et al., Accurate modelling of fabricated hollow-core photonic bandgap fibers, *Opt. Exp.* 23 (18) (2015) 23117–23132.
- [10] T.D. Bradley, X. Wang, E.N. Fokoua, et al., Measuring the group velocity dispersion of higher order modes in hollow core photonic bandgap fibre, *ECOC* (2015).
- [11] M. Napierala, E. Beres-Pawlik, T. Nasilowski, et al., Photonic crystal fiber with large mode area and characteristic bending properties, *IEEE Photon. Technol. Lett.* 24 (16) (2012) 1409–1411.
- [12] L. Wang, S.Q. Lou, W.G. Chen, H.L. Li, A novel method of rapidly modeling optical properties of actual photonic crystal fibres, *Chin. Phys. B* 19 (8) (2010) 1–7.
- [13] Y. Shen, S.Q. Lou, X. Wang, Estimation method of point spread function based on Kalman filter for accurately evaluating real optical properties of photonic crystal fibers, *Appl. Opt.* 53 (9) (2014) 1838–1845.
- [14] Y. Shen, X. Wang, S.Q. Lou, et al., Evaluation of optical properties for real photonic crystal fiber based on total variation in wavelet domain, *Opt. Fiber Technol.* 31 (2016) 1–12.
- [15] D.L. Donoho, Compressed sensing, *IEEE Trans. Inf. Theory* 52 (4) (2006) 1289–1306.
- [16] E.J. Candès, Y.C. Eldar, D. Needell, et al., Compressed sensing with coherent and redundant dictionaries, *Appl. Comput. Harmon. Anal.* 31 (1) (2010) 59–73.
- [17] C.A. Da, J. Zhou, M.N. Do, The nonsubsampling contourlet transform: theory, design, and applications, *IEEE Trans. Image Process.* 15 (10) (2006) 3089–3101.
- [18] J.F. Cai, Z. Shen, Image restoration: total variation, wavelet frames, and beyond, *J. Am. Math. Soc.* 25 (4) (2012) 1033–1089.
- [19] P. Getreuer, Total variation deconvolution using split Bregman, *Image Process. Line* 2 (2012) 158–174.
- [20] F. Wen, P. Liu, Y. Liu, et al., Robust sparse recovery in impulsive noise via L_p - L_1 optimization, *IEEE Trans. Image Process.* 65 (1) (2017) 105–118.
- [21] Y.L. Liu, T.B. Mi, S.D. Li, Compressed sensing with general frames via optimal-dual-based-analysis, *IEEE Trans. Inf. Theory* 58 (7) (2012) 4201–4214.
- [22] F. Poli, A. Cucinotta, S. Selleri, *Photonic Crystal Fibers: Properties and Applications*, 2013.